

Fore stalled Phase Separation as the Precursor to Stripe Order

Aritra Sinha¹ and Alexander Wietek¹

¹*Max Planck Institute for the Physics of Complex Systems,
Nöthnitzer Strasse 38, Dresden 01187, Germany*

(Dated: November 26, 2024)

Stripe order is a prominent feature in the phase diagram of the high-temperature cuprate superconductors and has been confirmed as the ground state of the two-dimensional Fermi Hubbard model in certain parameter regimes. Upon increasing the temperature, stripes and the superconducting state give way to the enigmatic strange metal and pseudogap regime, whose precise nature poses long-standing, unresolved puzzles. Using modern tensor network techniques, we discover a crucial aspect of these regimes. Infinite projected entangled pair state (iPEPS) simulations in the fully two-dimensional limit reveal a maximum in the charge susceptibility at temperatures above the stripe phase. This maximum is located around hole-doping $p = 1/8$ and intensifies upon cooling. Using minimally entangled typical thermal states (METTS) simulations on finite cylinders, we attribute the enhanced charge susceptibility to the formation of charge clusters, reminiscent of phase separation where the system is partitioned into hole-rich and hole-depleted regions. In contrast to genuine phase separation, the charge cluster sizes fluctuate statistically without a divergent charge susceptibility. Hence, while this precursor state features clustering of charge carriers, true phase separation is ultimately forestalled at lower temperatures by the onset of stripe order.

In the context of high- T_c superconductors (HTSCs), phase separation refers to the segregation of a uniformly doped system into hole-rich metallic and hole-depleted antiferromagnetic regions [1, 2]. Experimental findings demonstrate that some HTSCs exhibit such charge inhomogeneities. These include early discoveries of phase separation in $\text{La}_2\text{CuO}_{4+\delta}$ by Grenier et al. [3] and the subsequent identification of stripe order, i.e., intertwined charge and spin order, in the copper oxide $\text{La}_{1.6-x}\text{Nd}_{0.4}\text{Sr}_x\text{CuO}_4$ (with $x = 0.12$) by Tranquada et al. in 1995 [4]. Beyond cuprate superconductors [5–7], phase separation has been found recently in materials like iron-based chalcogenides [8, 9], doped manganites [10], and nickelates [11]; see Ref. [12] for a recent review. Prior to these discoveries, research on phase separation in cuprate superconductors has primarily focused on its role in superconductivity [1, 2]. Early mean-field theories suggest that doped charge carriers form clusters, which evolve into metallic networks that are essential for superconductivity [1, 13, 14]. The theoretical concepts of charge density waves (CDW) and stripe order in cuprates [15–18] emerged alongside ideas about phase separation and electronic inhomogeneities in these materials [19]. This includes the work of Emery and Kivelson on frustrated phase separation [20], where it was argued that long-range Coulomb repulsion might play a key role in breaking up macroscale phase separation into CDW-like order. Experimental discoveries of CDWs in cuprates [4] were tied into this picture. Recently, theoretical studies on phase separation have regained attention, focusing on Hubbard-Holstein and related models, which include both electron and phonon interactions [21–23].

The square lattice two-dimensional (2D) Fermi-Hubbard model (FHM) [24] stands as a fundamental model for interacting electrons on a lattice, crucial for understanding high-temperature superconductivity [25–27]. The model with nearest-neighbor (NN) hopping, is described by the

Hamiltonian:

$$H = -t \sum_{\langle i,j \rangle, \sigma} c_{i\sigma}^\dagger c_{j\sigma} + \text{h.c.} + U \sum_i n_{i\uparrow} n_{i\downarrow}, \quad (1)$$

where t represents the NN hopping amplitude and $U > 0$ denotes the on-site Coulomb repulsion. Here, $c_{i\sigma}^\dagger$ ($c_{i\sigma}$) is the creation (annihilation) operator for an electron with spin σ at site i , and $n_{i\sigma} = c_{i\sigma}^\dagger c_{i\sigma}$ is the number operator for electrons of spin σ at site i . The summation $\langle i, j \rangle$ runs over NN sites on the square lattice. In this article, we set $t = 1$. The phase diagram of these models has been the subject of intense debate for decades [28, 29]. Recently, a consensus has emerged among most numerical methods that, when the model is constrained to nearest-neighbor (NN) electron hopping, the ground state for the slightly doped case is the stripe order under conditions relevant to cuprates [30–38]. The pseudogap and strange metal phenomena in cuprate superconductors, which emerge at higher temperatures before the stripe order and superconductivity, have spurred extensive studies on the finite-temperature behavior of the Hubbard model [39–44]. Notable findings include a cellular dynamical mean-field theory (CDMFT) study [40], which shows that short-range spin correlations contribute to additional spectral bands, suppressing momentum-dependent spectral weight and forming the pseudogap. Recently, diagrammatic Monte Carlo simulations [44] attributed the pseudogap mainly to spin correlations, with limited influence from charge fluctuations. Another study [43] reinforced the spin origin of the pseudogap, while highlighting that charge inhomogeneities may play some role.

This work explores the parameter regimes of the Fermi-Hubbard model at finite temperatures and slight doping, specifically where the pseudogap and strange metal regimes occur. We employ state-of-the-art tensor network techniques—the minimally entangled typical thermal states (METTS) [45, 46] with matrix product states

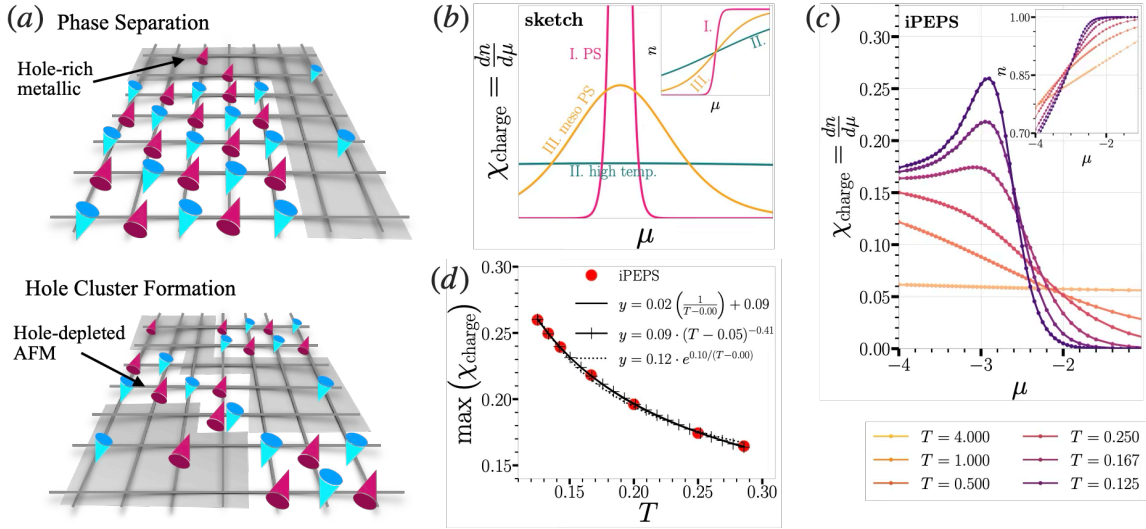


FIG. 1. **Charge Susceptibility.** (a) Cartoon illustrations of phase separation in the Fermi-Hubbard model on a square lattice. The top panel shows complete phase separation, with a hole-rich phase (shaded grey) and an antiferromagnetic (AFM) domain (unshaded), with red and blue cones representing spin-up and spin-down polarization of the electrons. The bottom panel depicts hole clustering, where thermal fluctuations prevent complete phase separation, resulting in clusters of holes accompanied by AFM domains. (b) Schematic of charge susceptibility χ_{charge} vs. chemical potential μ , depicting three possible scenarios: **I** (pink curve) indicates sharp phase separation at the ground state, with a discontinuity in n (inset) and a divergent peak in χ_{charge} ; **II** (green curve) represents high-temperature behavior with smoothed n vs. μ and flat χ_{charge} ; and **III** (orange curve) displays near-critical behavior at finite temperature, with a peak in χ_{charge} . (c) iPEPS simulations on an infinite square lattice at $U = 10$ reveal a shift from Scenario **II** to **III** as temperature T decreases from $T = 4$ to $T = 0.125$. (d) The peak value in charge susceptibility χ_{charge} from (c) as a function of temperature. Linear fit with $1/(T - T')$ (solid black line) and polynomial fit with $(T - T')^\gamma$ (solid black line with plus markers) are the best fits and suggest divergence of χ_{charge} as $T \rightarrow T_c \geq 0$.

(MPS)[47, 48] ansatz, and purification [49] with infinite projected entangled pair states (iPEPS) [50, 51] ansatz. The iPEPS with purification allows us to explore infinite 2D systems effectively in the thermodynamic limit, which complements MPS with METTS, suited for studying 1D and quasi-1D systems like finite-width cylinders at lower temperatures. Our simulations reveal a novel aspect of matter in this regime: the onset of charge clustering facilitated by antiferromagnetism at intermediate temperatures, suggesting an imminent phase separation. However, phase separation is ultimately forestalled by the emergence of stripe order at lower temperatures.

To simulate the system, we initially implement the purification method [52] with fermionic iPEPS [51] following Ref. [53]. Here we use the particle-hole symmetric form of the FHM,

$$H = - \sum_{\langle i,j \rangle \sigma} t \left(c_{i\sigma}^\dagger c_{j\sigma} + c_{j\sigma}^\dagger c_{i\sigma} \right) + \sum_i U \left(n_{i\uparrow} - \frac{1}{2} \right) \left(n_{i\downarrow} - \frac{1}{2} \right) - \sum_i \mu n_i. \quad (2)$$

We control the filling n by changing the chemical potential μ . In this grand-canonical formalism, the system exchanges particles with a reservoir, and the particle density n adjusts to reach equilibrium, leading to a unique equilibrium density for a given chemical potential. The charge susceptibility $\chi_{\text{charge}} = \frac{\partial n}{\partial \mu}$ quantifies

how sensitive the particle density is to changes in the chemical potential. The sketch Fig. 1(b) illustrates three scenarios with χ_{charge} versus μ plots and density n versus μ plots (inset). Scenario **I** (pink curve) shows a sharp phase separation at ground state for some $\mu = \mu_c$ with a sharp discontinuity in the n vs μ plot and a divergent peak in χ_{charge} , suggesting enhanced susceptibility. This signature has been used to provide evidence for phase separation in iPEPS studies of fermions on square and honeycomb lattices [51, 54]. Scenario **II** (green curve) describes a high-temperature state with substantial thermal fluctuations that smoothes the n vs μ curve and keeps χ_{charge} relatively flat. There exists a scenario **III** (orange curve), which demonstrates a subdued phase transition at finite temperatures. Here, the n vs μ curve exhibits a noticeable change in curvature without a discontinuous jump. The charge susceptibility χ_{charge} in this case shows a modest peak, signifying an increased, but finite, susceptibility to variations in μ . We will later see that in the Hubbard model it can be caused due to statistically fluctuating hole clusters that mimic phase separation on a smaller scale without achieving full phase separation. Cartoon illustrations of Scenario **I** and **III** for the Fermi-Hubbard model are presented in Fig. 1(a), with Scenario **I** depicted at the top and Scenario **III** at the bottom. Here, Fig. 1(c) presents calculations done with iPEPS for an infinite square lattice at $U = 10$ and shows a gradual shift from scenario **II** to **III** as we change the tempera-

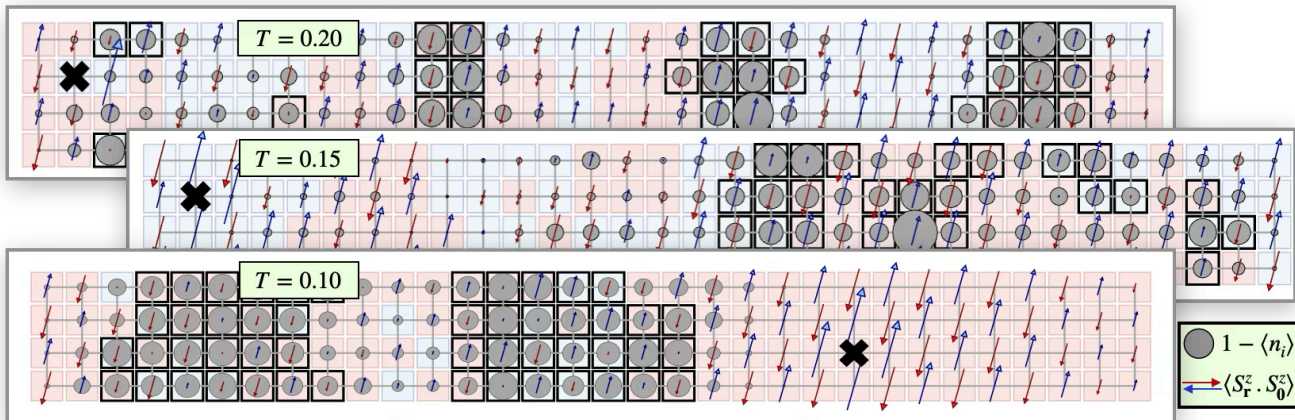


FIG. 2. **METTS snapshots.** Visualizations of hole density and spin correlations for a typical METTS state $|\psi_i\rangle$ in the Hubbard model with $U = 10$ at electron density $n = 0.9375$ on a 32×4 cylinder. Grey circles, with diameters proportional to hole densities $1 - \langle n_l \rangle = 1 - \langle \psi_i | n_l | \psi_i \rangle$, highlight variations in local charge distribution. Spin correlations are shown by arrows (red for negative and blue for positive) of lengths proportional to the correlation strengths $\langle \psi_i | S_0^z \cdot S_l^z | \psi_i \rangle$; black cross denotes the origin $l = 0$ of the spin correlator. Red and blue squares mark the sign and spatial structure of staggered spin correlations, $(-1)^{x+y} \langle \psi_i | S_0^z \cdot S_l^z | \psi_i \rangle$ and thus assigns the same color to each site within a given antiferromagnetic domain. Panels from top to bottom display snapshots at temperatures $T = 0.20$, $T = 0.15$, and at $T = 0.10$. As the temperature drops, larger hole clusters and enhanced AFM domains appear, though no stripe order is observed. Black-bordered sites indicate hole densities exceeding a specified threshold (Eq. 5), with neighboring black-bordered sites forming the clusters \mathcal{C}_l in Eq. 8.

ture T from $T = 4$ to $T = 0.125$. Fig. 1(d) plots the maxima of χ_{charge} of Fig. 1(c) as a function of temperature. We tested three kinds of fit, linear with $1/(T - T')$ given as solid black line; a polynomial fit with $|T - T'|^\gamma$ given as a solid black line with plus markers and an exponential fit which goes as $\exp(h/|T - T'|)$, where h is a constant and given as a dotted line. Both the linear and polynomial fits align well with the iPEPS data, implying that χ_{charge} may diverge at some critical temperature $T \rightarrow T_c \geq 0$. This behavior is consistent with findings from dynamical cluster approximation (DCA) [55, 56] for the Hubbard model with the next-nearest neighbor coupling $t' = 0$. It was shown there that χ_{charge} does not diverge at finite temperatures but shows signs of divergence as $T \rightarrow 0$. In the presence of finite t' , however, the Hubbard model was shown to undergo a first-order phase separation transition at finite temperatures, terminating at a second-order critical point where χ_{charge} diverges. This critical point aligns with a quantum critical point ($T = 0$) at $t' = 0$, separating pseudogap and Fermi-liquid regions. Sordi et al. [57] connect this behavior to the Widom line, a line of maxima in χ_{charge} that extends from the QCP, but mapped in our article in the χ_{charge} vs. T framework rather than across the U - T plane. The Widom line represents a thermodynamic crossover boundary, organizing the phase space and marking the onset of the pseudogap phase at a characteristic temperature T^* .

Simulations employing iPEPS at finite temperature in the grand-canonical ensemble typically result in a uniform particle density across the system due to choice of a translationally invariant ansatz. While for studies done with the canonical ensemble using METTS [45, 46],

fixes the total number of particles. Thereby charge inhomogeneities can be readily observed. Here, we follow the methodologies outlined in Ref. [58]. Unless otherwise specified, we conducted our simulations primarily on a cylindrical lattice with length $L = 32$ (open boundary conditions along the length) and width $W = 4$ (periodic boundary conditions along the width). Using the same on-site Coulomb repulsion as in the previous iPEPS study ($U = 10$), we set the electron filling to $n = 0.9375$. The METTS algorithm, a Markov chain Monte Carlo method, simulates thermal states via iterative imaginary-time evolution of product states [45, 46]. The evolution process involves creating METTS snapshots $|\psi_i\rangle$,

$$|\psi_i\rangle = \frac{1}{\sqrt{p_i}} e^{-\beta H/2} |\sigma_i\rangle, \quad (3)$$

where $|\sigma_i\rangle$ denotes the basis of product states, $p_i = \langle \sigma_i | e^{-\beta H} | \sigma_i \rangle$, and $\beta = 1/T$ the inverse temperature. By averaging over the individual observables calculated via snapshot wavefunctions $|\psi_i\rangle$, we estimate the thermal observables:

$$\begin{aligned} \langle O \rangle &= \frac{1}{Z} \text{Tr}(e^{-\beta H} O) \\ &= \frac{1}{Z} \sum_i \langle \sigma_i | e^{-\beta H/2} O e^{-\beta H/2} | \sigma_i \rangle \\ &= \frac{1}{Z} \sum_i p_i \langle \psi_i | O | \psi_i \rangle, \end{aligned} \quad (4)$$

where Z is the partition function given by $Z = \sum_i p_i$. Hole densities and spin correlations can be calculated directly from these snapshots. In representative typical

snapshots in Fig. 2, we observe at $T = 0.20$ (top panel), $T = 0.15$ (middle panel) and $T = 0.10$ (bottom panel), large hole clusters and pronounced antiferromagnetic domains, indicative of strong hole clustering. Hole densities at a lattice site l are calculated as $1 - \langle \psi_i | n_l | \psi_i \rangle$, where $n_l = n_{l\uparrow} + n_{l\downarrow}$. Spin correlations are illustrated by red and blue arrows of length proportional to $\langle \psi_i | S_l^z \cdot S_m^z | \psi_i \rangle$. To represent staggered domains, the squares denoting lattice sites are color-coded; regions with staggered correlations are shaded in one color, with adjacent staggered domains differing by a π -phase shift shown in the alternate color (either red or blue). As we examine the typical snapshots, it becomes evident that, as thermal fluctuations diminish with decreasing temperature, the system increasingly favors the formation of more extensive antiferromagnetic domains. These strong fluctuations reflect the system's proximity to an instability leading to stripe formation. For clustering in lattices of larger width, see Fig. 7 of appendix B. However, at $T = 0.025$, we observe regular charge density wave patterns with a wavelength of $6 \sim 8$ lattice sites (not shown here; see Fig. 8 of appendix B or references [58, 59] for a typical snapshot showing stripe order) instead of a fully formed phase separation.

To capture the clustering behavior, we employ an algorithm to statistically analyze the hole clusters in the METTS snapshots. Let's define the set of all lattice sites in a METTS snapshot $|\psi_i\rangle$ as Λ . Each snapshot is scrutinized to identify sites where the local hole density n_h exceeds a specified threshold. This threshold n_h^{th} is defined as

$$n_h^{\text{th}} = 1 - n + c\sigma. \quad (5)$$

where $1 - n$ is the mean hole density, σ is the standard deviation of the hole density distribution within a METTS snapshot $|\psi_i\rangle$,

$$\sigma = \sqrt{\frac{1}{|\Lambda|} \sum_{s \in \Lambda} (n_h(s) - (1 - n))^2}, \quad (6)$$

where $|\Lambda|$ is the total number of lattice sites. Here, c is a sensitivity parameter set to $c = 0.5$ to balance between detecting meaningful clusters and avoiding sensitivity to individual site variations. We refer to appendix C to check the robustness of clustering analysis against other values of c . Next we examine the hole-density of one given METTS snapshot to identify the subset of sites \mathcal{E} where the hole density $n_h(s)$ exceeds the threshold n_h^{th} :

$$\mathcal{E} = \{s \in \Lambda \mid n_h(s) > n_h^{\text{th}}\}. \quad (7)$$

We partition \mathcal{E} into disjoint clusters \mathcal{C}_l , where each cluster $\mathcal{C}_l \subseteq \Lambda$ is a maximal connected component of sites satisfying $n_h(s) > n_h^{\text{th}}$ for all $s \in \mathcal{C}_l$:

$$\mathcal{E} = \bigcup_l \mathcal{C}_l. \quad (8)$$

Each cluster, indexed by l , can be associated with two quantities: the cluster size $C_l = |\mathcal{C}_l|$, representing the

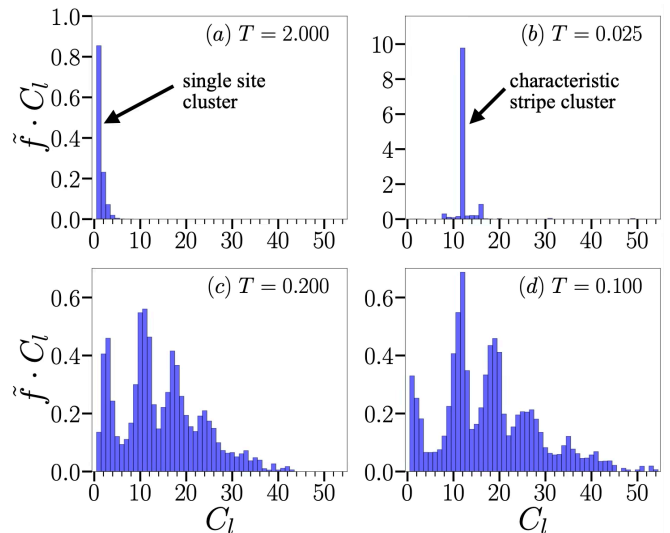


FIG. 3. **Clustering in METTS snapshots.** The plot shows the product of the normalized frequency distributions and hole cluster sizes, $\tilde{f}(C_l) \cdot C_l$, versus cluster size C_l for different temperatures at $U = 10$ and filling $n = 0.9375$. At higher temperatures, such as $T = 2$ shown in panel (a), predominantly small clusters (single-site, $C_l = 1$) are observed, indicating strong thermal fluctuations. In contrast, at lower temperatures ($T = 0.2$ in panel (c) and $T = 0.1$ in panel (d)), larger clusters become more prevalent, suggesting increased hole clustering as thermal fluctuations decrease. Panel (b) at $T = 0.025$ illustrates the dominance of a specific cluster size ($C_l = 12$), hinting at the onset of a regularized charge density wave order.

number of sites within the cluster, and the cluster weight $W_l = \sum_{s \in \mathcal{C}_l} n_h(s)$, representing the total hole density of the cluster. From each snapshot, we output a set of (C_l, W_l) pairs for all clusters identified within that snapshot. To obtain a comprehensive view of the clustering structure across the entire ensemble, we aggregate (C_l, W_l) values from all METTS snapshots generated via the sampling process. From this aggregate, we define the normalized frequency $\tilde{f}(C_l)$ as

$$\tilde{f}(C_l) = \frac{\sum_{\text{snapshots}} \sum_{\mathcal{C}_l: |\mathcal{C}_l|=C_l} W_l}{\sum_{\text{snapshots}} \sum_{\mathcal{C}_l} W_l}, \quad (9)$$

where the numerator sums the weights W_l of all clusters of size C_l across all snapshots, and the denominator is the total weight of all clusters extracted from all snapshots. This quantity $\tilde{f}(C_l)$ thus represents the relative prevalence of clusters of size C_l , averaged over the METTS ensemble. These frequency distributions multiplied by the cluster sizes $\tilde{f}(C_l) \cdot C_l$, plotted in Fig. 3, highlight interesting features. At higher temperatures $T = 2$ (Fig. 3(a)), almost no large clusters are formed due to enhanced thermal fluctuations; a single-site cluster, i.e., $C_l = 1$, is the most dominant. At lower temperatures, $T = 0.2$ (Fig. 3(c)) and $T = 0.1$ (Fig. 3(d)), larger clusters dominate showing a broad spread in cluster sizes. At

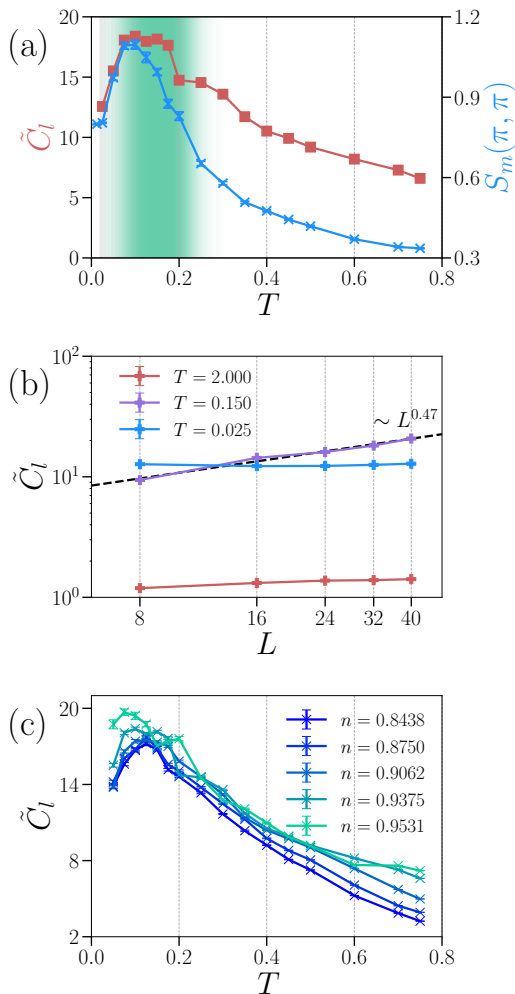


FIG. 4. **Temperature dependence of clustering and magnetic ordering in the Fermi-Hubbard model.** (a) The mean cluster size \tilde{C}_l , weighted by normalized frequencies $\tilde{f}(C_l)$, and the spin structure factor $S_m(\mathbf{k})$ at $\mathbf{k} = (\pi, \pi)$ as a function of temperature T for $U = 10$ and electron density $n = 0.9375$ (same parameters for (b)). We see approximately correlated peaks in the antiferromagnetic ordering and cluster size at intermediate temperatures (the correlated peaks are shaded in teal color). (b) System size dependence of mean cluster size, $\tilde{C}_l(L)$ for different temperatures in a log-log scale. We find power law scaling of increase in $\tilde{C}_l(L)$ at $T = 0.15$ in the charge clustering regime, while at high temperatures ($T = 2.000$) and at very low temperatures ($T = 0.025$) when stripe phase sets in, we see no system-size dependence. (c) Maximum clustering behavior at intermediate temperatures is observed over a range of densities from $n = 0.84375$ to $n = 0.95312$.

very low temperatures $T = 0.025$, $C_l = 12$ is the dominant one, corresponding to charge density wave order.

We further calculate the mean cluster size \tilde{C}_l , weighted by the normalized frequencies $\tilde{f}(C_l)$, as

$$\tilde{C}_l = \sum_{C_l} C_l \cdot \tilde{f}(C_l),$$

and plot it as a function of temperature in Fig. 4(a). Additionally, we compute the magnetic structure factor, defined as

$$S_m(\mathbf{k}) = \frac{1}{N} \sum_{l,m=1}^N e^{i\mathbf{k} \cdot (\mathbf{r}_l - \mathbf{r}_m)} \langle S_l^z \cdot S_m^z \rangle. \quad (10)$$

Here, \mathbf{r}_l denotes the coordinate of the l -th lattice point, and $\mathbf{k} = (k_x, k_y)$ denotes the quasi-momentum in reciprocal space. In particular, we focus on the spin structure factor $S_m(\mathbf{k})$ at $\mathbf{k} = (\pi, \pi)$, which denotes antiferromagnetic correlations. \tilde{C}_l , alongside $S_m(\mathbf{k})$ at $\mathbf{k} = (\pi, \pi)$ in Fig. 4(a), reveals that the peaks in cluster sizes and antiferromagnetic ordering at intermediate temperatures are approximately correlated. This correlation indicates that large hole clustering is accompanied by antiferromagnetic domains which enhances the magnetic structure factor at $\mathbf{k} = (\pi, \pi)$, a behavior characteristic of phase separation in the Fermi-Hubbard model.

In Fig. 4(b), we show the mean cluster sizes $\tilde{C}_l(L)$ for cylindrical lattice sizes of different lengths $L = 8, 16, 24, 32$ and 40 , and same width $W = 4$ for temperatures $T = 2, 0.15$ and 0.025 . While for $T = 0.15$ which is in the charge clustering regime we see a commensurate dependence on size, at high ($T = 2$) and very low temperatures ($T = 0.025$), there is almost no size-dependence. For the latter, $\tilde{C}_l(L)$ is locked at a value of around 12, characterizing the stripe cluster size. In Fig. 4(c), we show that this typical maxima in clustering behavior at intermediate temperatures range across a wide range of fillings $n = 0.8438, \dots, n = 0.9531$. We applied a bootstrap analysis to get an estimate of the error in case of the mean cluster sizes.

Finally, we explore a more conventional approach to detecting phase separation. In Fig. 5, we present the charge structure factor,

$$S_c(\mathbf{k}) = \frac{1}{N} \sum_{l,m=1}^N e^{i\mathbf{k} \cdot (\mathbf{r}_l - \mathbf{r}_m)} \langle (n_l - n)(n_m - n) \rangle \quad (11)$$

for a filling of $n = 0.9375$, considering various system sizes of lengths $L = 16, 24, 32$, and 40 , with a fixed width $W = 4$. Note that, since we are working in the canonical ensemble, $S_c(\mathbf{k} = 0) = 0$, because there is no fluctuation in total density at zero momentum. At a temperature $T = 0.15$, an inner peak is present at the lowest momentum mode $\mathbf{k} = (\frac{2\pi}{L}, 0)$ resolved by the lattice, which shifts inward as the system size increases. Physically, this inward shift with system size indicates a build-up of long-wavelength density fluctuations, characteristic of phase separation. This trend is highlighted by dotted orange lines marking peak positions in both the main plot and inset. The inset further amplifies the inner peaks corresponding to different system sizes, using darker shades to represent larger sizes. As the temperature decreases to $T = 0.025$, the system transitions into a stripe phase, characterized by a pronounced peak at $\mathbf{k} = (\frac{\pi}{4}, 0)$ (illustrated by a blue dashed line) that remains consistent across different system sizes.

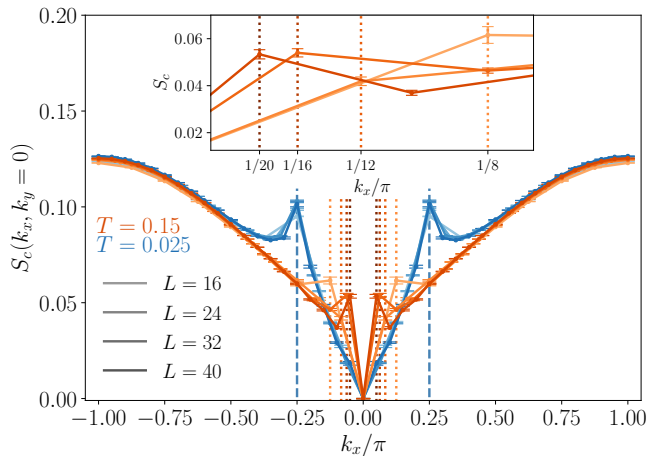


FIG. 5. **Charge Structure Factors.** Charge structure factor $S_c(\mathbf{k})$ (Eq. 11) for electron density $n = 0.9375$ and $U = 10$ across system sizes of length $L = 16, 24, 32, 40$ and width $W = 4$. It manifests a subtle inner peak at $\mathbf{k} = (\frac{2\pi}{L}, 0)$ at temperature $T = 0.15$ resolved by the lattice length. It shifts inward with increasing L , suggesting a commensurate charge order (dotted orange lines). The inset highlights these shifts with darker shades for larger sizes. At $T = 0.025$, the emergence of a stripe phase is marked by a stable peak at $\mathbf{k} = (\frac{\pi}{4}, 0)$ (blue dashed line) consistent across different system sizes.

DISCUSSION

In this study, we employed advanced tensor network simulations to explore the thermal phase diagram of the two-dimensional Fermi-Hubbard model, focusing on regimes where pseudogap and strange metallic behavior are anticipated. Our simulation results reveal an intriguing progression: at intermediate temperatures, the system shows a propensity for phase separation, marked by hole clustering and the formation of antiferromagnetic (AFM) domains. However, as temperature decreases, these clusters are prevented from merging into a fully phase-separated state. Instead, stripe order emerges, suggesting that fluctuations linked to an incipient stripe order might have been steering the system's behavior at elevated temperatures—an instability that becomes increasingly prominent as temperatures drop. The rise in charge susceptibility observed in our iPEPS simulations, which intensifies with decreasing temperature, lends further support to this interpretation. The onset of antiferromagnetic correlations have previously been tied to the formation of a pseudogap in numerous works [43, 44, 58–61]. Now, we discover that, additionally, the onset of antiferromagnetic correlations favors the formation of hole clusters as shown in Fig. 4. The clustering also clearly manifests itself in susceptibility towards phase separation, where the charge structure factor develops a small peak at the smallest momentum k resolved by the lattice in the canonical ensemble, cf. Fig. 5. Intuitively, antiferromagnetic correlations can be maxi-

mized whenever exactly two electrons reside on nearest-neighbor sites, and hence, strong antiferromagnetic correlations favor half-filled regions. Thus, an attraction between electrons mediated by antiferromagnetic correlations depletes other regions of the system, which constitute the hole-rich clusters. Notably, experimental techniques such as resonant inelastic X-ray scattering (RIXS) observed high-temperature precursor charge density wave (PCDW) fluctuations and stripe correlations in cuprate superconductors, supporting the idea that charge fluctuations play a significant role in the pseudogap regime [62–65]. These findings motivate us to propose a connection between our observations and the pseudogap phenomenon in high-temperature cuprate superconductors. Within the AFM domains, strong spin correlations and electron localization introduce a gap in the electronic spectrum, leading to insulating behavior. Adjacent hole-rich metallic regions introduce low-energy states that partially fill this gap, suppressing the density of states at the Fermi level without creating a full gap—an iconic feature of the pseudogap phase. While an exhaustive exploration of this phenomenon is outside the scope of the current study, our results suggest that the interaction between AFM ordering and metallicity arising from hole clustering could play a pivotal role in the development of the pseudogap. In the t - J model, when the exchange coupling $J/t \geq 1$, the ground state is known to phase-separate [66, 67]. Recent studies done in this regime observed that under long time evolution, the charge degrees of freedom remain completely frozen [68]. This could be related to the large resistivity encountered in cuprates in the pseudogap, strange and bad metal regimes.

METHODS

Solving the FHM presents substantial challenges due to its strongly interacting nature; analytical solutions are rare and limited to specific cases [69, 70]. Even the most advanced numerical methods often face difficulties in accurately solving the model without biases from approximation schemes [71]. For finite temperature, the minimally entangled typical thermal states (METTS) algorithm, when applied to MPS [45, 46] offers significant advantages over traditional methods like purification [49], notably in representing thermal states with lower bond dimensions. METTS has facilitated insightful studies into the thermal phase diagram of the square-lattice FHM including the study of the pseudogap regime and the stripe phase [58]. Similarly, purification techniques using iPEPS [72–75] have explored the phase diagram from high to intermediate temperatures, revealing significant distortions in antiferromagnetism upon doping [53]. Additionally, alternative approaches for finite temperature simulations using tensor networks for the Hubbard model include the exponential thermal tensor renormalization group (XTRG) [76], tangent space tensor renormalization group (tanTRG) [77], and METTS

applied to PEPS [78]. A recent study using diagrammatic Monte Carlo [79] was able to achieve temperatures as low as $T = 0.067$ and up to $U = 7$ for arbitrary large lattices, providing insights into momentum-resolved spin and charge susceptibilities. See Ref. [80] for a detailed list of methods approaching the FHM at finite temperatures. Complementing these computational breakthroughs, experimental techniques with ultracold atoms have similarly advanced, enabling precise simulation and investigation of many-body physics that echo the complex interactions found in the Hubbard model [81–87]. These experiments confine systems with hundreds of fermions and can reach temperatures as low as $1/4$ of the hopping energy, hosting non-trivial charge and spin correlations [88–93].

In this work, we utilize two tensor network (TN) methods to simulate the FHM, focusing on approaches that are constrained by entanglement entropy, typically characterized by the bond dimension D . The first method uses the infinite projected entangled pair states (iPEPS) ansatz, using the neighborhood tensor update (NTU) algorithm [94–96], as described in Ref. [53]. The iPEPS operates in the thermodynamic limit, effectively eliminating finite-size effects. We focus on local updates for iPEPS optimization, called the neighborhood tensor update (NTU) [96]. This method is computationally more efficient and numerically stable compared to global updates like the Full Update. Additionally, NTU provides greater accuracy than the Simple Update [97] which does mean-field-like approximations. The iPEPS approach we used simulates thermal states using the purification technique, which is broadly favored for finite-temperature simulations. In iPEPS, the purification of a thermal state is performed using a tensor network in which the thermal density matrix $\rho(\beta)$, representing the system at inverse temperature $\beta = 1/T$, is encoded as a pure state in an enlarged Hilbert space that includes both physical and ancillary degrees of freedom (d.o.f.). The process begins by representing the infinite temperature state as a product of maximally entangled states between corresponding local physical and ancillary d.o.f. This state serves as the starting point for imaginary-time evolution, implemented through a sequence of tensor network operations that progressively cool the system to the desired temperature. The thermal density matrix is then obtained by tracing out the ancillary degrees of freedom from the pure state representation. Mathematically, this is described by the equation:

$$\rho(\beta) = \text{Tr}_{\text{aux}} (|\psi(\beta)\rangle\langle\psi(\beta)|),$$

where $|\psi(\beta)\rangle$ is the state obtained after applying the imaginary-time evolution operator $e^{-\beta H/2}$ to the initial state, and Tr_{aux} denotes the partial trace over the ancillary degrees of freedom. In our simulations, we enforced $U(1) \times U(1)$ symmetry, which conserves particle number, using the YASTN package [98], optimized for fermionic and symmetric PEPS. This symmetry conservation helps to reduce computational overhead. With this approach, we

could go up to bond dimensions $D = 30$ and were able to explore temperatures as low as $T = 0.125$. However, the rapid growth of the bond dimension due to the entanglement introduced by purification limits iPEPS’s ability to access very low temperatures without significant computational cost.

The second method we employed is the minimally entangled typical thermal states (METTS) algorithm, which uses matrix product states (MPS) as the variational ansatz. METTS is especially effective in one-dimensional cylindrical geometries and excels at lower temperatures. Unlike purification, METTS does not require the full representation of the thermal density matrix. Instead, METTS relies on generating a sequence of typical thermal states through a Monte Carlo sampling process. The method works by selecting a product state, evolving it in imaginary time by $\beta/2$, and then collapsing the evolved state into a new product state using Markov chain sampling (see Eqn. 3 and Eqn. 4 of the main text). The imaginary time evolution in METTS is carried out using the time-dependent variational principle (TDVP) [99, 100], with subspace expansion [101], which helps improve the stability and accuracy of the evolution process. By avoiding the full tracking of the thermal density matrix, METTS can achieve accurate results with significantly lower bond dimensions than purification. Our METTS implementation, based on the ITensor library [102, 103], was able to reach bond dimensions up to $D = 2500$, particularly for systems on 32×4 cylinder geometries, following successful approaches from previous studies [58, 104]. Another notable advantage of METTS is its ability to provide spatially resolved data, which was key in identifying the clustering at intermediate temperatures.

ACKNOWLEDGMENTS

We thank Antoine Georges, George Batrouni, Salvatore Manmana, Roderich Moessner, Steve White, Luke Staszewski, Martin Ulaga, Joe H. Winter, Timon Hilker, Lode Pollet, Zhenjiu Wang, Thomas Chalopin, Immanuel Bloch, Fabian Grusdt and Annabelle Bohrdt for insightful discussions and in particular Fakher Assaad for highlighting the signatures of phase separation in the charge structure factor to us. We thank Chris Hoolley for suggesting the adjective “forestalled” and further discussions. A.W. acknowledges support by the DFG through the Emmy Noether program (Grant No. 509755282). A.S. thanks Marek M. Rams and Jacek Dziarmaga for previous technical discussions on iPEPS. A.S. acknowledges support from National Science Centre (NCN), Poland under project 2019/35/B/ST3/01028, at Jagiellonian University, Kraków, where part of the work was completed.

Appendix A: Convergence for iPEPS

To confirm convergence with respect to bond dimension, we compare charge compressibility $\chi_{\text{charge}} = \frac{dn}{d\mu}$ and electron density n at bond dimensions $D = 20$ and $D = 30$ in Fig. 6. There is close alignment between the results for two representative temperatures $T = 0.25$ and $T = 0.125$ at both bond dimensions across a range of μ for the values of χ_{charge} and n . This suggests that increasing the bond dimension further would yield minimal differences, validating the accuracy of our compressibility and density calculations for the interesting parameter ranges.

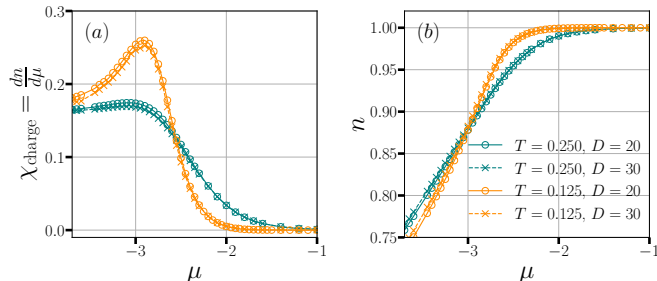


FIG. 6. **Convergence of Charge Compressibility and Density with Bond Dimension.** (a) Charge compressibility, $\chi_{\text{charge}} = \frac{dn}{d\mu}$, and (b) filling n as functions of chemical potential μ for bond dimensions $D = 20$ (circles) and $D = 30$ (crosses), at temperatures $T = 0.25$ (teal) and $T = 0.125$ (dark orange). The close agreement between $D = 20$ and $D = 30$ values indicates convergence in both χ_{charge} and n .

Appendix B: Additional Plots for METTS Cylinder

To see whether hole clustering happens for systems of larger cylinder width, we choose a cylinder of length $L = 16$ and $W = 6$. Converging larger-width cylinders

in MPS is challenging due to the increased entanglement entropy between the left and right halves of the system, which scales with the width. As the width grows, the number of entangled degrees of freedom increases, demanding a much higher bond dimension to faithfully capture this entanglement, leading to higher computational costs. For simulations of width 6, we used $D = 3000, 3500$ and 4000 to check convergence for energy per system size E/N and average double occupancy $\langle n_{\uparrow}n_{\downarrow} \rangle$ in Fig. 7 (a) and (b) and the data seems well converged till temperature $T = 0.15$. In Fig. 7(c), we plot a random METTS snapshot at $T = 0.15$. The black-bordered squares are those which are above a certain threshold density n_h^{th} defined in Eq. 5 in the main text, and they highlight the significant hole-clustering. We also notice the presence of antiferromagnetic domains.

Fig. 8 depicts a typical METTS snapshot at very low temperature $T = 0.025$ for a cylinder of size 32×4 where stripe order has set in. They form well-formed striped clusters of size 12 which is the dominating cluster size at low temperatures as found in Fig. 3(b) of the main text.

Appendix C: Robustness of definition of clusters

In the main text, clusters are identified in each METTS snapshot by locating sites where the hole density n_h exceeds the threshold $n_h^{\text{th}} = 1 - n + c\sigma$, where c is a coefficient that modulates the impact of the standard deviation σ of the hole density distribution. Figure 9 shows that, even when varying the coefficient c , the overall behavior of the mean cluster size \tilde{C}_l as a function of temperature remains robust. The threshold for cluster definition is slightly altered by changing c , but the general trends, with small clusters prevailing at higher temperatures and larger clusters dominating at lower temperatures, are unaffected. This demonstrates that the clustering analysis is not extremely sensitive to the specific choice of c , and the observed trends in cluster size versus temperature remain reliable across different threshold definitions. In the main text we set $c = 0.5$ to balance sensitivity to local density fluctuations.

-
- [1] E. Sigmund and K. A. Müller, Phase separation in cuprate superconductors: Proceedings of the second international workshop, [September 4-10, 1993, Cottbus, Germany \(2012\)](#).
 - [2] E. Dagotto, Correlated electrons in high-temperature superconductors, [Rev. Mod. Phys. 66, 763 \(1994\)](#).
 - [3] J.-C. Grenier, A. Wattiaux, and M. Pouchard, Phase separation in the superconducting $\text{La}_2\text{CuO}_{4+\delta}$ phases ($0 < \delta < 0.09$) prepared by electrochemical oxidation, [Phase Separation in Cuprate Superconductors , 187 \(1992\)](#).
 - [4] J. Tranquada, B. Sternlieb, J. Axe, Y. Nakamura, and S. Uchida, Evidence for stripe correlations of spins and

- holes in copper oxide superconductors, [Nature 375, 561 \(1995\)](#).
- [5] S. H. Pan, J. P. O'Neal, R. L. Badzey, C. Chamon, H. Ding, J. R. Engelbrecht, Z. Wang, H. Eisaki, S.-i. Uchida, A. K. Gupta, E. W. Hudson, K. M. Lang, and J. C. Davis, Microscopic electronic inhomogeneity in the high- T_c superconductor $\text{Bi}_2\text{Sr}_2\text{CaCu}_2\text{O}_{8+\delta}$, [Nature 413, 282 \(2001\)](#).
- [6] K. McElroy, J. Lee, J. Slezak, D.-H. Lee, H. Eisaki, S. Uchida, and J. C. Davis, Atomic-scale sources and mechanism of nanoscale electronic disorder in $\text{Bi}_2\text{Sr}_2\text{CaCu}_2\text{O}_{8+\delta}$, [Science 309, 1048 \(2005\)](#).

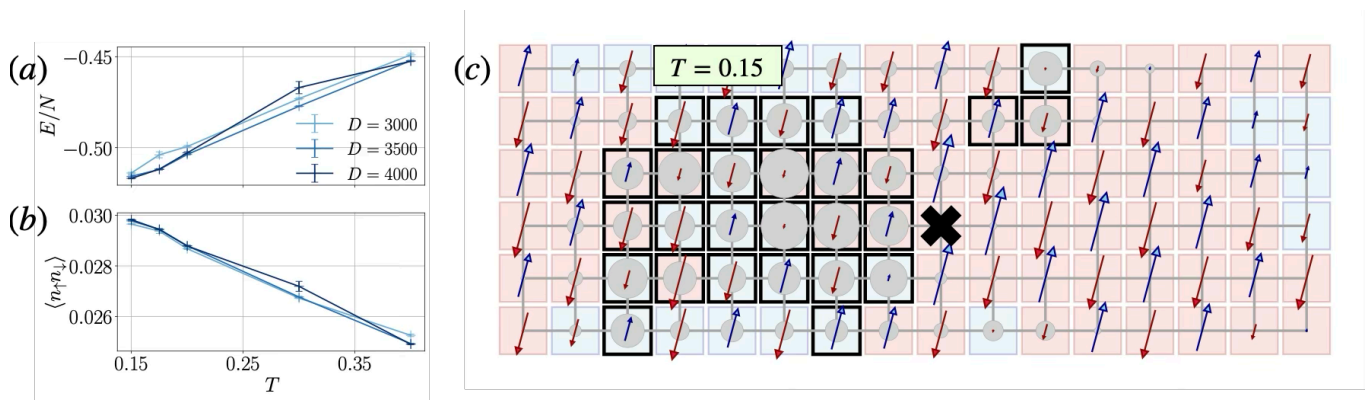


FIG. 7. **Larger Width Cylinder: METTS snapshot.** We provide energy (a) and double-occupancy (b) data for a 16×6 cylinder for filling $n = 0.9375$ at different temperatures and show its convergence with bond dimensions. At $T = 0.15$, the data seems well converged. In (c), we display a typical METTS snapshot for $T = 0.15$ following the convention as in Fig. 2 of the main text. We see large hole-clustering (squares with black-border have hole-densities greater than a threshold described in the main text) and large antiferromagnetic domains for most clusters at this temperature.

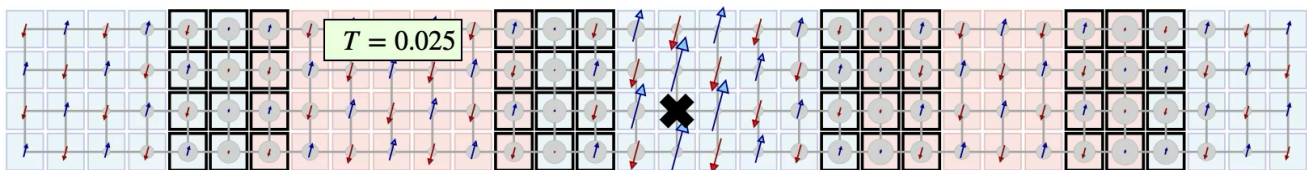


FIG. 8. **Charge Clustering at Low Temperatures.** We see a typical METTS snapshot for a 32×4 cylinder for electron density $n = 0.9375$ at temperature $T = 0.025$. We see well-formed charged density wave intertwined with antiferromagnetic domains which have π -phase shift in the middle of cluster. The typical cluster size in a striped phase is 12 which is shown by black-bordered neighboring high density sites.

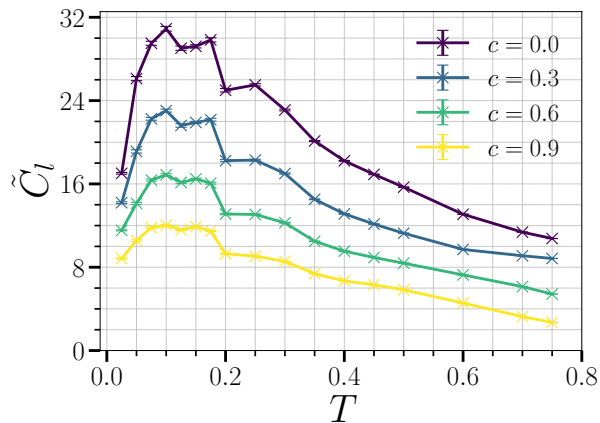


FIG. 9. **Robustness of definition of hole-clusters.** Mean hole cluster size \tilde{C}_l as a function of temperature T for various values of the coefficient c in the threshold $n_h^{\text{th}} = 1 - n + c\sigma$, which defines a hole cluster.

- [7] G. Campi, A. Bianconi, N. Poccia, G. Bianconi, L. Barba, G. Arrighetti, D. Innocenti, J. Karpinski, N. D. Zhigadlo, S. M. Kazakov, *et al.*, Inhomogeneity of charge-density-wave order and quenched disorder in a high- T_c superconductor, *Nature* **525**, 359 (2015).
- [8] R. Yuan, T. Dong, Y. Song, P. Zheng, G. Chen, J. Hu, J. Li, and N. Wang, Nanoscale phase separation of antiferromagnetic order and superconductivity in $\text{K}_{0.75}\text{Fe}_{1.75}\text{Se}_2$, *Sci. Rep.* **2**, 221 (2012).
- [9] A. Ricci, N. Poccia, G. Campi, B. Joseph, G. Arrighetti, L. Barba, M. Reynolds, M. Burghammer, H. Takeya, Y. Mizuguchi, Y. Takano, M. Colapietro, N. L. Saini, and A. Bianconi, Nanoscale phase separation in the iron chalcogenide superconductor $\text{K}_{0.8}\text{Fe}_{1.6}\text{Se}_2$ as seen via scanning nanofocused x-ray diffraction, *Phys. Rev. B* **84**, 060511 (2011).
- [10] T. Miao, L. Deng, W. Yang, J. Ni, C. Zheng, J. Etheridge, S. Wang, H. Liu, H. Lin, Y. Yu, *et al.*, Direct experimental evidence of physical origin of electronic phase separation in manganites, *Proc. Natl. Acad. Sci. U.S.A.* **117**, 7090 (2020).
- [11] G. Campi, A. Bianconi, B. Joseph, S. K. Mishra, L. Müller, A. Zozulya, A. A. Nugroho, S. Roy, M. Sprung, and A. Ricci, Nanoscale inhomogeneity of charge density waves dynamics in $\text{La}_{2-x}\text{Sr}_x\text{NiO}_4$, *Sci.*

- Rep. **12**, 15964 (2022).
- [12] M. Y. Kagan, K. Kugel, and A. Rakhmanov, Electronic phase separation: Recent progress in the old problem, *Phys. Rep.* **916**, 1 (2021).
- [13] V. Hizhnyakov and E. Sigmund, High- T_c superconductivity induced by ferromagnetic clustering, *Physica C* **156**, 655 (1988).
- [14] V. Hizhnyakov, N. Kristoffel, and E. Sigmund, On the percolation induced conductivity in high- T_c superconducting materials, *Physica C* **160**, 119 (1989).
- [15] J. Zaanen and O. Gunnarsson, Charged magnetic domain lines and the magnetism of high- T_c oxides, *Phys. Rev. B* **40**, 7391 (1989).
- [16] D. Poilblanc and T. M. Rice, Charged solitons in the Hartree-Fock approximation to the large- U Hubbard model, *Phys. Rev. B* **39**, 9749 (1989).
- [17] K. Machida, Magnetism in La_2CuO_4 -based compounds, *Physica C* **158**, 192 (1989).
- [18] J. Zaanen and A. M. Oleś, Striped phase in the cuprates as a semiclassical phenomenon, *Ann. Phys.* **508**, 224 (1996).
- [19] S. Caprara, The ancient romans route to charge density waves in cuprates, *Condens. Matter* **4**, 60 (2019).
- [20] V. J. Emery and S. Kivelson, Frustrated electronic phase separation and high-temperature superconductors, *Physica C* **209**, 597 (1993).
- [21] T. Ohgoe and M. Imada, Competition among Superconducting, Antiferromagnetic, and Charge Orders with Intervention by Phase Separation in the 2D Holstein-Hubbard model, *Phys. Rev. Lett.* **119**, 197001 (2017).
- [22] S. Julia-Farré, A. Dauphin, R. W. Chhajlany, P. T. Grochowski, S. Wall, M. Lewenstein, and P. R. Grzybowski, Nanoscale phase separation and pseudogap in the hole-doped cuprates from fluctuating Cu-O-Cu bonds, *Phys. Rev. B* **101**, 125107 (2020).
- [23] S. Karakuzu, A. Tanjaron Ly, P. Mai, J. Neuhaus, T. A. Maier, and S. Johnston, Stripe correlations in the two-dimensional Hubbard-Holstein model, *Commun. Phys.* **5**, 311 (2022).
- [24] J. Hubbard, Electron correlations in narrow energy bands, *Proc. R. Soc. Lond. A Math. Phys. Sci.* **276**, 238 (1963).
- [25] P. W. Anderson, The resonating valence bond state in La_2CuO_4 and superconductivity, *Science* **235**, 1196 (1987).
- [26] F. C. Zhang and T. M. Rice, Effective hamiltonian for the superconducting Cu oxides, *Phys. Rev. B* **37**, 3759 (1988).
- [27] V. J. Emery and G. Reiter, Mechanism for high-temperature superconductivity, *Phys. Rev. B* **38**, 4547 (1988).
- [28] C. S. Hellberg and E. Manousakis, Phase separation at all Interaction Strengths in the t - J Model, *Phys. Rev. Lett.* **78**, 4609 (1997).
- [29] S. R. White and D. J. Scalapino, Phase separation and stripe formation in the two-dimensional t - J model: A comparison of numerical results, *Phys. Rev. B* **61**, 6320 (2000).
- [30] B.-X. Zheng, C.-M. Chung, P. Corboz, G. Ehlers, M.-P. Qin, R. M. Noack, H. Shi, S. R. White, S. Zhang, and G. K.-L. Chan, Stripe order in the underdoped region of the two-dimensional Hubbard model, *Science* **358**, 1155 (2017).
- [31] S. R. White and D. J. Scalapino, Stripes on a 6-leg hubbard ladder, *Phys. Rev. Lett.* **91**, 136403 (2003).
- [32] G. Hager, G. Wellein, E. Jeckelmann, and H. Fehske, Stripe formation in doped hubbard ladders, *Phys. Rev. B* **71**, 075108 (2005).
- [33] B.-X. Zheng and G. K.-L. Chan, Ground-state phase diagram of the square lattice hubbard model from density matrix embedding theory, *Phys. Rev. B* **93**, 035126 (2016).
- [34] E. W. Huang, C. B. Mendl, S. Liu, S. Johnston, H.-C. Jiang, B. Moritz, and T. P. Devereaux, Numerical evidence of fluctuating stripes in the normal state of high- T_c cuprate superconductors, *Science* **358**, 1161 (2017).
- [35] E. W. Huang, C. B. Mendl, H.-C. Jiang, B. Moritz, and T. P. Devereaux, Stripe order from the perspective of the hubbard model, *npj Quantum Mater.* **3**, 22 (2018).
- [36] G. Ehlers, S. R. White, and R. M. Noack, Hybrid-space density matrix renormalization group study of the doped two-dimensional hubbard model, *Phys. Rev. B* **95**, 125125 (2017).
- [37] M. Qin, C.-M. Chung, H. Shi, E. Vitali, C. Hubig, U. Schollwöck, S. R. White, and S. Zhang (Simons Collaboration on the Many-Electron Problem), Absence of Superconductivity in the Pure Two-Dimensional Hubbard Model, *Phys. Rev. X* **10**, 031016 (2020).
- [38] Y.-F. Jiang, J. Zaanen, T. P. Devereaux, and H.-C. Jiang, Ground state phase diagram of the doped hubbard model on the four-leg cylinder, *Phys. Rev. Res.* **2**, 033073 (2020).
- [39] C. Huscroft, M. Jarrell, T. Maier, S. Moukouri, and A. N. Tahvildarzadeh, Pseudogaps in the 2d hubbard model, *Phys. Rev. Lett.* **86**, 139 (2001).
- [40] B. Kyung, S. S. Kancharla, D. Sénéchal, A.-M. S. Tremblay, M. Civelli, and G. Kotliar, Pseudogap induced by short-range spin correlations in a doped Mott insulator, *Phys. Rev. B* **73**, 165114 (2006).
- [41] E. Gull, O. Parcollet, and A. J. Millis, Superconductivity and the pseudogap in the two-dimensional hubbard model, *Phys. Rev. Lett.* **110**, 216405 (2013).
- [42] E. W. Huang, R. Sheppard, B. Moritz, and T. P. Devereaux, Strange metallicity in the doped hubbard model, *Science* **366**, 987 (2019).
- [43] M. Meixner, H. Menke, M. Klett, S. Heinzlmann, S. Andergassen, P. Hansmann, and T. Schäfer, Mott transition and pseudogap of the square-lattice Hubbard model: Results from center-focused cellular dynamical mean-field theory, *SciPost Phys.* **16**, 059 (2024).
- [44] F. Šimkovic IV, R. Rossi, A. Georges, and M. Ferrero, Origin and fate of the pseudogap in the doped Hubbard model, *Science* **385**, eade9194 (2024).
- [45] S. R. White, Minimally entangled typical quantum states at finite temperature, *Phys. Rev. Lett.* **102**, 190601 (2009).
- [46] E. Stoudenmire and S. R. White, Minimally entangled typical thermal state algorithms, *New J. Phys.* **12**, 055026 (2010).
- [47] M. Fannes, B. Nachtergaele, and R. F. Werner, Finitely correlated states on quantum spin chains, *Commun. Math. Phys.* **144**, 443 (1992).
- [48] S. Rommer and S. Östlund, Class of ansatz wave functions for one-dimensional spin systems and their relation to the density matrix renormalization group, *Phys. Rev. B* **55**, 2164 (1997).

- [49] F. Verstraete, J. J. Garcia-Ripoll, and J. I. Cirac, Matrix product density operators: Simulation of finite-temperature and dissipative systems, *Phys. Rev. Lett.* **93**, 207204 (2004).
- [50] J. Jordan, R. Orús, G. Vidal, F. Verstraete, and J. I. Cirac, Classical simulation of infinite-size quantum lattice systems in two spatial dimensions, *Phys. Rev Lett.* **101**, 250602 (2008).
- [51] P. Corboz, R. Orús, B. Bauer, and G. Vidal, Simulation of strongly correlated fermions in two spatial dimensions with fermionic Projected Entangled-Pair States, *Phys. Rev. B* **81**, 165104 (2010).
- [52] P. Czarnik, J. Dziarmaga, and P. Corboz, Time evolution of an infinite projected entangled pair state: An efficient algorithm, *Phys. Rev. B* **99**, 035115 (2019).
- [53] A. Sinha, M. M. Rams, P. Czarnik, and J. Dziarmaga, Finite-temperature tensor network study of the Hubbard model on an infinite square lattice, *Phys. Rev. B* **106**, 195105 (2022).
- [54] P. Corboz, S. Capponi, A. M. Läuchli, B. Bauer, and R. Orús, Comment on “Topological quantum phase transitions of attractive spinless fermions in a honeycomb lattice” by Poletti D. et al., *EPL* **98**, 27005 (2012).
- [55] A. Macridin, M. Jarrell, and T. Maier, Phase separation in the Hubbard model using the dynamical cluster approximation, *Phys. Rev. B* **74**, 085104 (2006).
- [56] E. Khatami, K. Mikelsons, D. Galanakis, A. Macridin, J. Moreno, R. T. Scalettar, and M. Jarrell, Quantum criticality due to incipient phase separation in the two-dimensional Hubbard model, *Phys. Rev. B* **81**, 201101 (2010).
- [57] G. Sordi, P. Sémon, K. Haule, and A.-M. Tremblay, Pseudogap temperature as a widom line in doped mott insulators, *Sci. Rep.* **2**, 547 (2012).
- [58] A. Wietek, Y.-Y. He, S. R. White, A. Georges, and E. M. Stoudenmire, Stripes, Antiferromagnetism, and the Pseudogap in the Doped Hubbard Model at Finite Temperature, *Phys. Rev. X* **11**, 031007 (2021).
- [59] B. Xiao, Y.-Y. He, A. Georges, and S. Zhang, Temperature Dependence of Spin and Charge Orders in the Doped Two-Dimensional Hubbard Model, *Phys. Rev. X* **13**, 011007 (2023).
- [60] O. Gunnarsson, T. Schäfer, J. P. F. LeBlanc, E. Gull, J. Merino, G. Sangiovanni, G. Rohringer, and A. Toschi, Fluctuation diagnostics of the electron self-energy: Origin of the pseudogap physics, *Phys. Rev. Lett.* **114**, 236402 (2015).
- [61] T. Schäfer, N. Wentzell, F. Šimkovic, Y.-Y. He, C. Hille, M. Klett, C. J. Eckhardt, B. Arzhang, V. Harkov, F. m. c.-M. Le Régent, A. Kirsch, Y. Wang, A. J. Kim, E. Kozik, E. A. Stepanov, A. Kauch, S. Andergassen, P. Hansmann, D. Rohe, Y. M. Vilck, J. P. F. LeBlanc, S. Zhang, A.-M. S. Tremblay, M. Ferrero, O. Parcollet, and A. Georges, Tracking the footprints of spin fluctuations: A multimethod, multimessenger study of the two-dimensional hubbard model, *Phys. Rev. X* **11**, 011058 (2021).
- [62] H. Miao, J. Lorenzana, G. Seibold, Y. Peng, A. Amorese, F. Yakhov-Harris, K. Kummer, N. B. Brookes, R. Konik, V. Thampy, *et al.*, High-temperature charge density wave correlations in $\text{La}_1.875\text{Ba}_0.125\text{CuO}_4$ without spin-charge locking, *Proceedings of the National Academy of Sciences* **114**, 12430 (2017).
- [63] H. Miao, D. Ishikawa, R. Heid, M. Le Tacon, G. Fabbris, D. Meyers, G. D. Gu, A. Q. R. Baron, and M. P. M. Dean, Incommensurate phonon anomaly and the nature of charge density waves in cuprates, *Phys. Rev. X* **8**, 011008 (2018).
- [64] H. Miao, R. Fumagalli, M. Rossi, J. Lorenzana, G. Seibold, F. Yakhov-Harris, K. Kummer, N. B. Brookes, G. D. Gu, L. Braicovich, G. Ghiringhelli, and M. P. M. Dean, Formation of incommensurate charge density waves in cuprates, *Phys. Rev. X* **9**, 031042 (2019).
- [65] R. Arpaia and G. Ghiringhelli, Charge order at high temperature in cuprate superconductors, *J. Phys. Soc. Jpn.* **90**, 111005 (2021).
- [66] S. Rommer, S. R. White, and D. J. Scalapino, Phase separation in t - J ladders, *Phys. Rev. B* **61**, 13424 (2000).
- [67] C. Shih, Y. Chen, and T. Lee, Revisit phase separation of the two-dimensional t - J model by the power-lanczos method, *J. Phys. Chem. Solids* **62**, 1797 (2001).
- [68] L. Staszewski and A. Wietek, Quench dynamics of stripes and phase separation in the two-dimensional t - J model, [arXiv:2410.16387](https://arxiv.org/abs/2410.16387) (2024).
- [69] E. H. Lieb and F. Y. Wu, Absence of mott transition in an exact solution of the short-range, one-band model in one dimension, *Phys. Rev. Lett.* **20**, 1445 (1968).
- [70] Y. Nagaoka, Ferromagnetism in a narrow, almost half-filled s band, *Phys. Rev.* **147**, 392 (1966).
- [71] M. Qin, T. Schäfer, S. Andergassen, P. Corboz, and E. Gull, The Hubbard model: A computational perspective, *Annu. Rev. Condens. Matter Phys.* **13**, 275 (2022).
- [72] P. Czarnik, L. Cincio, and J. Dziarmaga, Projected entangled pair states at finite temperature: Imaginary time evolution with ancillas, *Phys. Rev. B* **86**, 245101 (2012).
- [73] P. Czarnik and J. Dziarmaga, Fermionic projected entangled pair states at finite temperature, *Phys. Rev. B* **90**, 035144 (2014).
- [74] A. Kshetrimayum, M. Rizzi, J. Eisert, and R. Orús, Tensor Network Annealing Algorithm for Two-Dimensional Thermal States, *Phys. Rev. Lett.* **122**, 070502 (2019).
- [75] P. Czarnik, M. M. Rams, P. Corboz, and J. Dziarmaga, Tensor network study of the $m = \frac{1}{2}$ magnetization plateau in the Shastry-Sutherland model at finite temperature, *Phys. Rev. B* **103**, 075113 (2021).
- [76] B.-B. Chen, C. Chen, Z. Chen, J. Cui, Y. Zhai, A. Weichselbaum, J. von Delft, Z. Y. Meng, and W. Li, Quantum many-body simulations of the two-dimensional fermi-hubbard model in ultracold optical lattices, *Phys. Rev. B* **103**, L041107 (2021).
- [77] Q. Li, Y. Gao, Y.-Y. He, Y. Qi, B.-B. Chen, and W. Li, Tangent Space Approach for Thermal Tensor Network Simulations of the 2d Hubbard model, *Phys. Rev. Lett.* **130**, 226502 (2023).
- [78] A. Sinha, M. M. Rams, and J. Dziarmaga, Efficient representation of minimally entangled typical thermal states in two dimensions via projected entangled pair states, *Phys. Rev. B* **109**, 045136 (2024).
- [79] F. Šimkovic IV, R. Rossi, and M. Ferrero, Two-dimensional Hubbard model at finite temperature: Weak, strong, and long correlation regimes, *Phys. Rev. Res.* **4**, 043201 (2022).
- [80] J. P. F. LeBlanc, A. E. Antipov, F. Becca, I. W. Bulik, G. K.-L. Chan, C.-M. Chung, Y. Deng, M. Ferrero, T. M. Henderson, C. A. Jiménez-Hoyos, E. Kozik,

- X.-W. Liu, A. J. Millis, N. V. Prokof'ev, M. Qin, G. E. Scuseria, H. Shi, B. V. Svistunov, L. F. Tocchio, I. S. Tupitsyn, S. R. White, S. Zhang, B.-X. Zheng, Z. Zhu, and E. Gull (Simons Collaboration on the Many-Electron Problem), Solutions of the two-dimensional Hubbard Model: Benchmarks and Results from a Wide Range of Numerical Algorithms, *Phys. Rev. X* **5**, 041041 (2015).
- [81] T. Esslinger, Fermi-Hubbard physics with atoms in an optical lattice, *Annu. Rev. Condens. Matter Phys.* **1**, 129 (2010).
- [82] A. Bohrdt, L. Homeier, C. Reinmoser, E. Demler, and F. Grusdt, Exploration of doped quantum magnets with ultracold atoms, *Ann. Phys.* **435**, 168651 (2021), special issue on Philip W. Anderson.
- [83] W. S. Bakr, J. I. Gillen, A. Peng, S. Fölling, and M. Greiner, A quantum gas microscope for detecting single atoms in a Hubbard-regime optical lattice, *Nature* **462**, 74 (2009).
- [84] J. F. Sherson, C. Weitenberg, M. Endres, M. Cheneau, I. Bloch, and S. Kuhr, Single-atom-resolved fluorescence imaging of an atomic mott insulator, *Nature* **467**, 68 (2010).
- [85] C. Gross and W. S. Bakr, Quantum gas microscopy for single atom and spin detection, *Nat. Phys.* **17**, 1316 (2021).
- [86] L. W. Cheuk, M. A. Nichols, M. Okan, T. Gersdorf, V. V. Ramasesh, W. S. Bakr, T. Lompe, and M. W. Zwierlein, Quantum-gas microscope for fermionic atoms, *Phys. Rev. Lett.* **114**, 193001 (2015).
- [87] M. F. Parsons, F. Huber, A. Mazurenko, C. S. Chiu, W. Setiawan, K. Wooley-Brown, S. Blatt, and M. Greiner, Site-resolved imaging of fermionic ${}^6\text{Li}$ in an optical lattice, *Phys. Rev. Lett.* **114**, 213002 (2015).
- [88] M. Boll, T. A. Hilker, G. Salomon, A. Omran, J. Nespolo, L. Pollet, I. Bloch, and C. Gross, Spin-and density-resolved microscopy of antiferromagnetic correlations in Fermi-Hubbard chains, *Science* **353**, 1257 (2016).
- [89] M. F. Parsons, A. Mazurenko, C. S. Chiu, G. Ji, D. Greif, and M. Greiner, Site-resolved measurement of the spin-correlation function in the Fermi-Hubbard model, *Science* **353**, 1253 (2016).
- [90] T. A. Hilker, G. Salomon, F. Grusdt, A. Omran, M. Boll, E. Demler, I. Bloch, and C. Gross, Revealing hidden antiferromagnetic correlations in doped Hubbard chains via string correlators, *Science* **357**, 484 (2017).
- [91] J. Koepsell, J. Vijayan, P. Sompet, F. Grusdt, T. A. Hilker, E. Demler, G. Salomon, I. Bloch, and C. Gross, Imaging magnetic polarons in the doped Fermi-Hubbard model, *Nature* **572**, 358 (2019).
- [92] C. S. Chiu, G. Ji, A. Bohrdt, M. Xu, M. Knap, E. Demler, F. Grusdt, M. Greiner, and D. Greif, String patterns in the doped Hubbard model, *Science* **365**, 251 (2019).
- [93] J. Koepsell, D. Bourgund, P. Sompet, S. Hirthe, A. Bohrdt, Y. Wang, F. Grusdt, E. Demler, G. Salomon, C. Gross, *et al.*, Microscopic evolution of doped mott insulators from polaronic metal to fermi liquid, *Science* **374**, 82 (2021).
- [94] F. Verstraete and J. I. Cirac, Renormalization algorithms for quantum-many body systems in two and higher dimensions, *arXiv:cond-mat/0407066* (2004).
- [95] M. Lubasch, J. I. Cirac, and M.-C. Bañuls, Algorithms for finite projected entangled pair states, *Phys. Rev. B* **90**, 064425 (2014).
- [96] J. Dziarmaga, Time evolution of an infinite projected entangled pair state: Neighborhood tensor update, *Phys. Rev. B* **104**, 094411 (2021).
- [97] R. Orús, A practical introduction to tensor networks: Matrix product states and projected entangled pair states, *Ann. Phys.* **349**, 117 (2014).
- [98] M. M. Rams, G. Wójtowicz, A. Sinha, and J. Hasik, **YASTN: Yet Another Symmetric Tensor Networks; A Python library for abelian symmetric tensor network calculations** (2024), source code available at <https://github.com/yastn/yastn>.
- [99] J. Haegeman, J. I. Cirac, T. J. Osborne, I. Pižorn, H. Verschelde, and F. Verstraete, Time-dependent variational principle for quantum lattices, *Phys. Rev. Lett.* **107**, 070601 (2011).
- [100] S. Paeckel, T. Köhler, A. Swoboda, S. R. Manmana, U. Schollwöck, and C. Hubig, Time-evolution methods for matrix-product states, *Ann. Phys.* **411**, 167998 (2019).
- [101] M. Yang and S. R. White, Time-dependent variational principle with ancillary krylov subspace, *Phys. Rev. B* **102**, 094315 (2020).
- [102] M. Fishman, S. R. White, and E. M. Stoudenmire, Codebase release 0.3 for ITensor, *SciPost Phys. Codebases*, 4 (2022).
- [103] M. Fishman, S. R. White, and E. M. Stoudenmire, The ITensor Software Library for Tensor Network Calculations, *SciPost Phys. Codebases*, 4 (2022).
- [104] A. Wietek, R. Rossi, F. Šimkovic, M. Klett, P. Hansmann, M. Ferrero, E. M. Stoudenmire, T. Schäfer, and A. Georges, Mott Insulating States with Competing Orders in the Triangular Lattice Hubbard Model, *Phys. Rev. X* **11**, 041013 (2021).